chemistry

MDPI

Article

Incorporating C_3N_5 and $NiCo_2S_4$ to Form a Novel Z-Scheme Heterojunction for Superior Photocatalytic Degradation of Norfloxacin

Sahil Rana [1], Amit Kumar [1,*], Tongtong Wang [2,*], Pooja Dhiman [1], Gaurav Sharma [1] and Hui Shi [2]

[1] International Research Centre of Nanotechnology for Himalayan Sustainability (IRCNHS), Shoolini University, Solan 173229, India; sahilrana987.sr@gmail.com (S.R.); dhimanpooja85@gmail.com (P.D.); gaurav8777@gmail.com (G.S.)

[2] Interdisciplinary and Innovate Research, Xi'an University of Architecture and Technology, Xi'an 710055, China; shihui@xauat.edu.cn

* Correspondence: mittuchem83@gmail.com (A.K.); wangtongtong@xauat.edu.cn (T.W.)

Abstract: Due to a combination of increased urbanization, industrialization, and population growth, many pharmaceutical pollutants are currently being discharged into the environment. A possible strategy is critical for eliminating antibiotic pollutants from the environment, and photocatalysis has been generally recognized as an excellent method for successfully degrading antibiotics at a faster pace. In this work, we employed a hydrothermal synthesis approach to create a novel $C_3N_5/NiCo_2S_4$ Z-scheme-based heterojunction with better interfacial charge transfer and used it as a catalyst for the degradation of norfloxacin antibiotic. The optimized 1:1 $C_3N_5/NiCo_2S_4$ (50CN/NCS) shows the highest photocatalytic efficiency of 86.5% in 120 min towards the degradation of norfloxacin (NOR). Such an effective performance can be attributed to the high responsive nature of photocatalyst in the visible region and superior transfer of interfacial charges via Z-scheme transfer in heterojunction. The high charge transfer efficiency and reduced recombination of charge carriers in heterojunction was confirmed by EIS and PL results. The influence of some key factors such as pollutant concentration, catalyst dosage, pH, and coexisting ions on the photocatalytic activity is also investigated in this work. The optimized heterojunction 50CN/NCS also degraded 89.1%, 78.3%, and 93.2% removal of the other pollutants CIP, SDZ, and BPA, respectively.

Keywords: Z-scheme; antibiotic; norfloxacin; photocatalysis; C_3N_5; heterojunction

check for updates

Citation: Rana, S.; Kumar, A.; Wang, T.; Dhiman, P.; Sharma, G.; Shi, H. Incorporating C_3N_5 and $NiCo_2S_4$ to Form a Novel Z-Scheme Heterojunction for Superior Photocatalytic Degradation of Norfloxacin. *Chemistry* **2024**, *6*, 962–980. https://doi.org/10.3390/chemistry6050056

Academic Editors: Vincenzo Vaiano and Olga Sacco

Received: 30 July 2024
Revised: 30 August 2024
Accepted: 3 September 2024
Published: 10 September 2024

Copyright: © 2024 by the authors. Licensee MDPI, Basel, Switzerland. This article is an open access article distributed under the terms and conditions of the Creative Commons Attribution (CC BY) license (https://creativecommons.org/licenses/by/4.0/).

1. Introduction

Among the biggest environmental problems faced by India and even the entire world today, antibiotic contamination is of great concern. Each year, India uses many tons of antibiotic medications for the treatment of humans, poultry, and cattle. The majority of antibiotic medications, however, are not entirely digested in both people and animals, and they are instead eliminated from the system via feces as their actual and efficient metabolites. The discharged antibiotic metabolites still possess biological functions and may contribute to environmental pollution. So, it is important to look into how antibiotics degrade [1,2]. In addition to the acute water contamination, the longevity and difficult-to-degrade characteristics of antibiotics will lead to the development of drug resistance, which will cause substantial environmental difficulties [3]. Advanced oxidation processes (AOPs) are popular methods for the high-performance removal of various water contaminants [4,5]. Because of its high mineralization, energy efficiency, and benign reaction conditions, AOP-based semiconductor photocatalysis has proven to be highly beneficial for energy and environmental applications [6,7]. Several photocatalysts including g-C_3N_4 [8], metal sulfides [9], and numerous semiconductors have been developed and manufactured in the past ten years for treatment of polluted water. However, there are still a number of major obstacles to overcome including the quick recombination

of light-induced electron–hole (e^-–h^+) pairs in substances, the lack of reactive sites over the surface, and the low degree of renewability because of photo-corrosion [10].

Because of its outstanding thermal/chemical durability, intriguing photoelectronic characteristics, and less toxic and abundant source, the carbon nitride class (for example, C_3N_4, C_2N_3, C_3N_5, and C_6N_7) has become an emerging player in photocatalysis [11–13]. In particular, C_3N_5 with larger nitrogen content, a newly created carbon nitride photocatalyst, has shown good prospects in visible-light-promoted photocatalytic hydrogen evolution, mitigating nitric oxide and recurrent organic pollutants because of its superior sunray absorption (E_g = 2.0 eV) and longer negative conduction band (CB) potential comparative to well-known g-C_3N_4 [14,15]. C_3N_5 is advantageous for organic pollutant adsorption and fast charge transfer to metal co-catalysts, and it possesses higher stability and robustness, which helps in avoiding secondary contamination [16]. However, due to an inherent flaw in the band structure, the extreme electron–hole recombination and inadequate redox capabilities of C_3N_5 hinder its capacity to function as a photocatalyst. It is important to develop a unique C_3N_5-based photocatalyst system that combines excellent redox capability with effective charge-carrier dissociation. Constructing heterojunctions with an oxidation semiconductor with a highly positive valence band (VB) potential and a reduction semiconductor with a highly negative conduction band (CB) potential has become a popular method to create highly efficient photocatalysts while simultaneously maintaining the highest redox ability [17]. In this respect, Z-scheme heterojunctions have been quite popular and advantageous because of high charge carrier separation and high redox capacity [18].

Hence, a possible method for improving the photocatalytic activity is to combine C_3N_5 to an oxidative semiconductor to create heterojunction with structural flaws. Various heterojunctions of C_3N_5, such as P-C_3N_4/C_3N_5 [19], FeS_2/g-C_3N_5 [20], etc., have been reported for photocatalytic pollutant removal and energy production. In recent years, spinel sulfides (AB_2S_4) were employed to activate PMS and eliminate organic contaminants. As an illustration, Xu et al. for the first time degraded bisphenol S in water by activating PMS using spinel sulfide mineral carrollite ($CuCo_2S_4$) [21]. The substitution of sulfur for oxygen can result in spinel sulfides having a greater deal of flexibility than spinel oxides due to lesser electronegativity of sulfur [22]. In bimetallic sulfides, sulfur acts as an electron donor, which may encourage the reduction–oxidation cycling of metal ions. Because of the wider redox reactions and synergistic impact of being bimetallic, these spinel sulfides function more catalytically than single-component sulfides [23]. $NiCo_2S_4$ is a bimetallic sulfide that has higher conductivity than Co and Ni alone, as well as high metal active sites to support a variety of catalytic processes. $NiCo_2S_4$ benefits from a strong absorption coefficient, larger carrier density, cost-effectiveness, the absence of hazardous elements, the absence of photo-driven decay, etc. As a result, it can serve as a substitute for valuable metals in photocatalysis reactions. Its surely an interesting idea to form a heterojunction between $NiCo_2S_4$ and C_3N_5. On the basis of the above-discussed considerations, a direct Z-scheme C_3N_5/$NiCo_2S_4$ heterojunction was successfully designed and prepared. Its performance for NOR removal was investigated under visible light. Meanwhile, the effects of factors such as NOR concentration, catalyst dosage, and initial pH on NOR removal were tested. Finally, a plausible NOR degradation pathway photocatalytic mechanism was also analyzed.

2. Experimental Section

2.1. Materials

3-amino-1,2,4-triazole (3-AT, 98%), ammonium chloride (NH_4Cl, 99%), nickel nitrate hexahydrate ($Ni(NO_3)_26H_2O$, 99%), cobalt nitrate hexahydrate ($Co(NO_3)_2.6H_2O$, 98%), thioacetamide (CH_4N_2S, 99%), and polyvinyl pyrrolidone $(C_6H_9NO)_n$ were all purchased from the Loba Chemie Pvt. Ltd. Mumbai, India and used without any further purification.

2.2. Synthesis of C_3N_5

Carbon nitride (C_3N_5) was prepared by a simple calcination method at high temperature. In brief, 3-amino-1,2,4-triazole (5 g) and ammonium chloride (5 g) were taken in a beaker and mixed uniformly to form a homogeneous mixture. Then, this mixture was transferred into a silica crucible and kept in a muffle furnace at 550 °C for 3 h. The crucible was allowed to cool at room temperature, and the obtained product was grounded in a mortar and pestle into a fine powder. This was denoted as C_3N_5 or roughly as CN. The C_3N_5 samples were orange in color, which is quite distinct from the yellow color of pristine g-C_3N_4 (Figure 1).

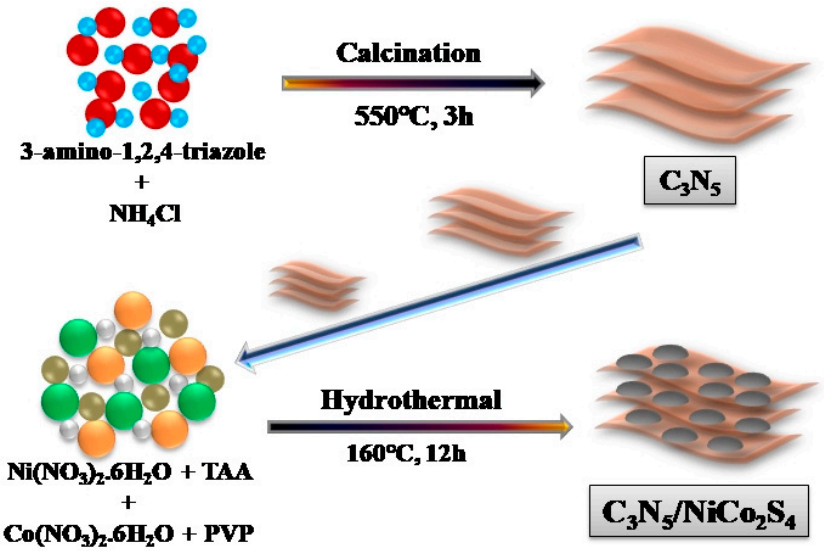

Figure 1. Hydrothermal synthesis method of $C_3N_5/NiCo_2S_4$ heterojunction.

2.3. Synthesis of $NiCo_2S_4$

The nickel cobalt sulfide was prepared by using the hydrothermal method. In total, 0.305 g of $Ni(NO_3)_2.6H_2O$, 0.610 g of $Co(NO_3)_2.6H_2O$, and 0.4 g of PVP were added into 40 mL of distilled water in a beaker and kept under stirring for 30 min to dissolve uniformly. After this, 0.819 g of CH_4N_2S was added into the above solution and again stirred for 30 min. After complete dissolution, the solution was transferred into a 100 mL Teflon-lined stainless-steel autoclave, Shilpent, India and heated in the muffle furnace at 160 °C for 12 h. The autoclave was allowed to cool at room temperature, and the obtained product was centrifuged 2–3 times with distilled water. The final product was obtained by drying at 80 °C in a hot air oven and marked as NCS.

2.4. Synthesis of $C_3N_5/NiCo_2S_4$ Heterojunction

The heterojunction of $C_3N_5/NiCo_2S_4$ was prepared through hydrothermal technique. First, 300 mg of C_3N_5 and 300 mg of $NiCo_2S_4$ were added to 50 mL of distilled water and were put to ultrasonication for 20 min. After complete mixing over magnetic stirring for one hour, the solution was transferred to a 100 mL Teflon-lined stainless steel autoclave and heated at 160 °C for 6 h. After cooling at room temperature, the particles were collected through centrifugation and dried in an electric oven at 60 °C. This was marked as 50% $C_3N_5/NiCo_2S_4$ (50CN/NCS). Similarly, 10% $C_3N_5/NiCo_2S_4$ (10CN/NCS), 20% $C_3N_5/NiCo_2S_4$ (20CN/NCS), 30% $C_3N_5/NiCo_2S_4$ (30CN/NCS), and 40% $C_3N_5/NiCo_2S_4$ (40CN/NCS) ratios were prepared using the same in-situ hydrothermal method. Figure 1 depicts the synthesis process of C_3N_5, $NiCo_2S_4$, and the $C_3N_5/NiCo_2S_4$ heterojunction.

2.5. Characterization

The X-ray diffraction (XRD) patterns of the samples were obtained through a 400 MHz Bruker diffractometer, Karlsruhe, Germany. By using the X-ray diffraction technique,

crystal structures and phase composition of materials were identified and examined. UV–Vis diffuse reflectance spectra were analyzed by Shimadzu UV-1900i spectrophotometer, Japan with 200–800 nm range to study the optical properties of the materials. FESEM images were obtained through a Hitachi SU8010 series field emission scanning electron microscope, Tokyo, Japan, and HRTEM images were obtained using JEOL JEM 2100 plus a high-resolution transmission electron microscope, Germany. FESEM and HRTEM were used to study the surface morphology and microstructures of the materials. The FESEM mapping was utilized to obtain the distribution of elements in the given composition. By using a Thermofisher scientific Nexsa base X-ray Photoelectron Spectroscope (XPS), the elemental composition of materials was examined, and surface electronic states were identified. Photoluminescence (PL) spectroscopy was analyzed through a Shimadzu RF-5301PC fluorescence spectrophotometer, Japan (excitation wavelength = 350 nm). Fourier transform infrared (FTIR) spectrum was analyzed on a Perkin Elmer infrared spectrometer Massachusetts, United States. The apparent flat band potential, transient photocurrent response, and Nyquist plots were assessed using a three-electrode setup on an electrochemical workstation (CHI660E).

2.6. Photocatalytic Activity

The photocatalytic performance of the material was carried out in a photochemical reactor for the degradation of antibiotic norfloxacin (NOR). Firstly, 40 mg of the catalyst was added into a 100 mL solution of NOR with a concentration of 20 mg L^{-1}. Then, to attain adsorption–desorption equilibrium, this solution was continuously agitated for 30 min in the dark. A 500 W Xenon (Xe) lamp was used as a visible light irradiation source, and the temperature of the photo-reactor in a quartz reaction vessel was maintained at around 25 °C using a water circulation system. At regular time intervals, the absorbance was noted using the by Shimadzu UV-1900i spectrophotometer, Japan to determine the residual concentration. The absorption maxima for NOR at 273 nm was used for the monitoring [24]. The NOR degradation intermediates were detected using a high-performance liquid chromatography–mass spectrometry using LC–MS, RRLC/6410B, QQQ instrument. A C18 column was used, and electron spray positive (ESI^+) ion mode was carried out. Free radical scavenger tests using certain sacrificial agents such as EDTA (h^+), IPA($^\bullet OH$), and BQ($^\bullet O_2^-$) were also carried out to determine the functions played by reactive species in the photocatalytic removal technique.

3. Results and Discussion

3.1. XRD Analysis

The structural characterization of the photocatalyst was determined using X-ray diffraction, and a framework for the qualitative, as well as quantitative, interpretation of the XRD data was acquired (Figure 2). The XRD pattern for C_3N_5 shows two peaks. The presence of conjugated CN in the structure is confirmed by the crystallinity of peak and alignment between layers [25]. A small peak at 13.1° provided proof that the structural arrangement was in-plane. Because of the lower diffraction peak at 13.1 (corresponding to 100 planes), it was proven that interlayer packing had been released and that planar size had decreased [25]. The peak can be clearly seen in the zoomed portion of the CRD for C_3N_5 and in the separate XRD plot in Figure S2. The diffraction peak at 27.55° for the 002 plane corresponds to the interphase stacking of the heptazine units. As C_3N_5 has more π-electrons as compared to g-C_3N_4, the layers in the former are more strongly attracted to each other by π–π interaction [26]. Thus, the 002 peak of C_3N_5 was shifted to a higher diffraction angle [27]. The characteristic diffraction peaks of $NiCo_2S_4$ obtained at 27.6°, 31.7°, 37.7°, 47.8°, and 54.4° match with the established standards, which correspond to the (220), (311), (400), (422), and (440) crystal planes of $NiCo_2S_4$ (JCPDS card No. 20-0782). The crystal structure of $NiCo_2S_4$ is indexed as a cubic spinel, which belongs to the Fd-3m space group. The lattice parameter calculated from (311) peak was found to be 9.31 Å with a lattice volume of 809.42 $Å^3$. The extra peaks obtained at 20.4° and 22.1° may be due

to the hexagonal phase Ni_3S_2 (JCPDS card No. 44-1418) [28]. The sharp diffraction peak obtained at 29.3° corresponds to the (311) plane of Co_9S_8 (JCPDS card No. 73-1442) due to the partial substitution of Co ions by Ni ions affecting only the lattice parameters and not the crystal structure [29]. In the $C_3N_5/NiCo_2S_4$ heterojunction, the peaks of both C_3N_5 and $NiCo_2S_4$ were simultaneously observed, which signifies the successful synthesis of the materials. The peaks for the Co_9S_8 phase are highly diminished in the heterojunction. The XRD patterns confirm the formation of the $C_3N_5/NiCo_2S_4$ heterojunction.

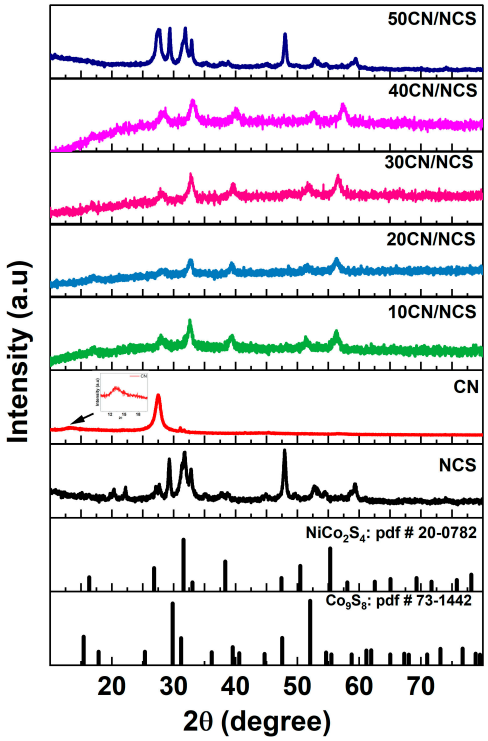

Figure 2. (XRD patterns of synthesized materials.

3.2. FTIR Analysis

The bonding and formation of the heterojunction were further confirmed by the FTIR analysis. Figure 3a displays the FTIR spectra of pure C_3N_5, $NiCo_2S_4$, and $C_3N_5/NiCo_2S_4$ heterojunction. The peaks are obtained for C_3N_5 at 803.62 cm^{-1}, 1231.61 cm^{-1}, 1402.83 cm^{-1}, and 3099.57 cm^{-1}. The sharp peak obtained at 803.62 cm^{-1} corresponds to the triazine rings as its basic framework [30]. The two peaks obtained in the range of 1200–1700 cm^{-1}, i.e., 1231.61 cm^{-1} and 1402.83 cm^{-1}, correspond to the C-N heterocycle stretching modes in the triazole rings. The peak at the 3099 cm^{-1} is due to the N-H stretching vibration [31]. Because of some remnant $-NH_2$ near the polymeric system's border, relatively weak wide peaks also appear [32]. An additional peak at 2180.68 cm^{-1} is ascribed to -C≡N (cyano groups), which are converted from $-C-NH_2$ (terminal groups) in melon structural units of C_3N_5 [33], supporting its formation.

Similarly, the peaks obtained for the pure $NiCo_2S_4$ material are at 454.5 cm^{-1}, 576 cm^{-1}, 1062.99 cm^{-1}, and 1608.41 cm^{-1}. Here, the peaks obtained at 454.5 cm^{-1}, 576 cm^{-1} (symmetrical stretch), and 1062.99 cm^{-1} (asymmetrical stretch) are attributed to the Co-S or Ni-S vibrations of the compound, which are crucial for the redox reactions [34]. The peak at 1608.41 cm^{-1} corresponds to the C=O stretching vibrations [35]. The FTIR spectra of CN/NCS heterojunction show the simultaneous existence of peaks of CN and NCS, indicating that the heterojunction has been successfully built. The peaks obtained for the 50CN/NCS are at 456.76 cm^{-1}, 576 cm^{-1}, 799.99 cm^{-1}, 1061.27 cm^{-1}, 1231.28 cm^{-1}, 1401.73 cm^{-1}, 1619.97 cm^{-1}, and 3060.68 cm^{-1}. The peaks at 799.99 cm^{-1}, 1231.28 cm^{-1},

1401.73 cm^{-1}, and 3060.68 cm^{-1} correspond to C_3N_5, and the peaks at 456.76 cm^{-1}, 576 cm^{-1}, 1061.27 cm^{-1}, and 1619.97 cm^{-1} correspond to $NiCo_2S_4$ material.

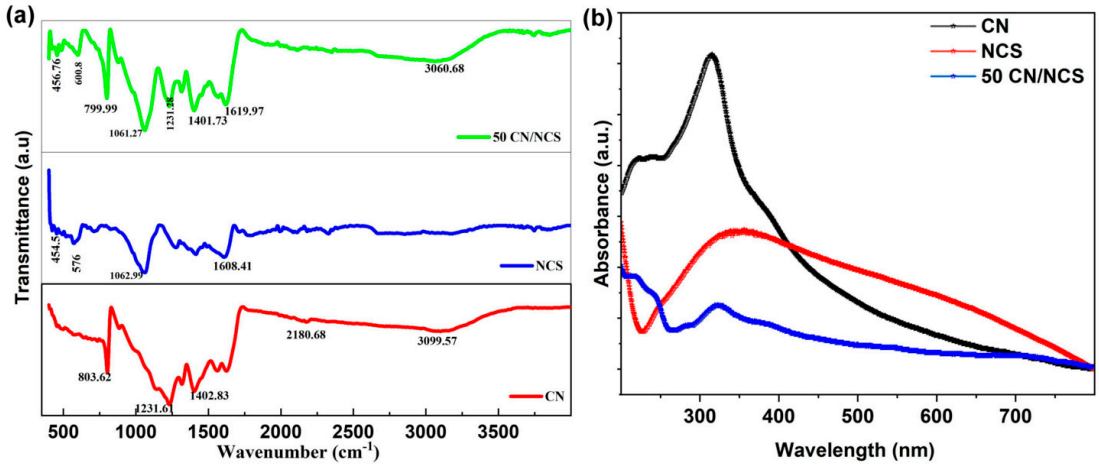

Figure 3. (**a**) FTIR spectra; (**b**) UV–DRS spectra of materials.

3.3. UV–DRS Analysis

The UV–Vis DRS studies were carried out to investigate the optical response of the materials. Using the Tauc's plots, the band gap energy of the synthesized samples was determined. The spectra and corresponding Tauc plots for the samples are shown in Figure 3b and Figure S3, respectively. The Shimadzu 1900i UV–Vis spectrophotometer was used to capture the adsorption spectra of the prepared samples in the 200–800 nm range. C_3N_5 shows a red shift of absorption edge to nearly 650 nm (unlikely for g-C_3N_4) because of an extended π-conjugated network, owing to an overlap of N 2p orbitals of bridging azo groups, and N 2p in a heptazine π-conjugated system [32]. It can be found from the spectra that the $NiCo_2S_4$ has a broader absorption range in the visible region as compared to the C_3N_5. Thus, NCS is more responsive in visible light than CN. The band gap of C_3N_5 as estimated from the Tauc plot is found to be 1.95 eV. This band gap is very close to, or we can say in between, as found by Yin et al. (1.80 eV) [36] and Mortazavi et al. (2.12 eV) [37].

On the other hand, spinel bimetallic sulfides have a relatively lower optical band gap, as low as 1.25 eV, as also reported by Sahoo et al. [38]. The band gap of NCS in this study was found to be 1.82 eV. The optical band of 50CN/NCS heterojunction was found to be 1.43 eV, lower than both the semiconductor materials.

3.4. FESEM and TEM Analysis

The morphology and the dimensions of prepared photocatalysts were investigated using the FESEM and HRTEM analysis. Figure 4a shows the FESEM image of the C_3N_5 catalyst. With numerous layers convergent into a big flat arrangement, the final structure simulates into a layered pattern that results into a layered sheet structure. The $NiCo_2S_4$ nanoparticles are nearly spherical and just have marginally formed particle-type morphology. The distribution lies in a range of 30–60 nm. The surface of this sample is rougher, porous, and made up of tightly packed nanoparticles as shown in the FESEM image in Figure 4b. The $NiCo_2S_4$ porous structure can result in a higher surface area, which is a huge benefit for samples to attain enhanced photocatalytic activity.

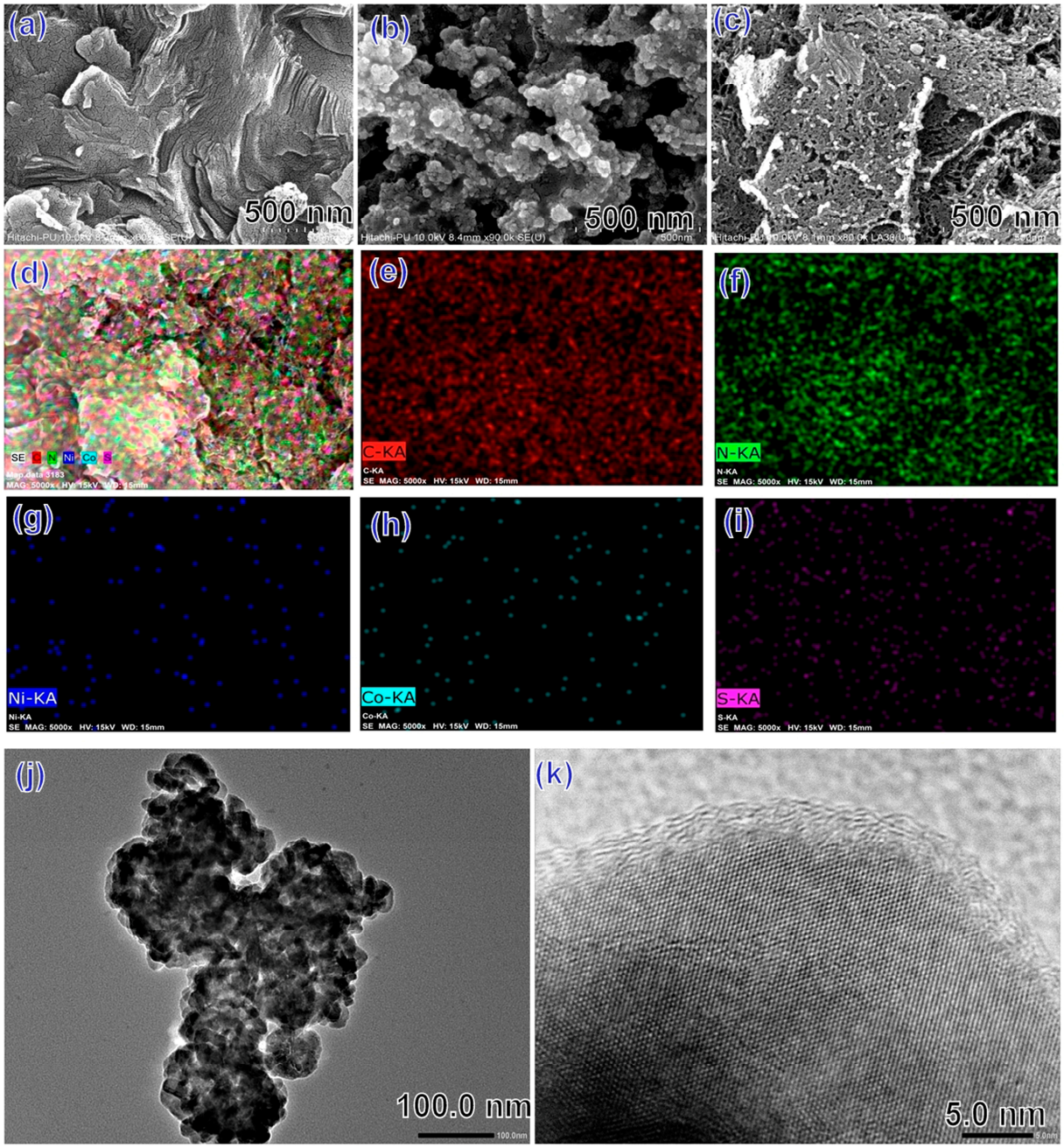

Figure 4. (**a**) FESEM images of C_3N_5; (**b**) FESEM images of $NiCo_2S_4$; (**c**) FESEM images of 50 CN/NCS; (**d**–**i**) Elemental mapping for 50 CN/NCS heterojunction; (**j**,**k**) TEM and HRTEM images for 50CN/NCS heterojunction.

The FESEM images of $C_3N_5/NiCo_2S_4$ heterojunction in Figure 4c show the layered pattern of C_3N_5 combined with the rougher and porous spherical nanoparticles of $NiCo_2S_4$. Also, there seems to be tight interfacial contact between the two materials, which is important for the successful construction of the heterojunction. The elemental mapping (Figure S4) analysis was performed to obtain the distributed elements in the 50CN/NCS heterojunction, and C, N, Ni, Co, and S were successfully identified as shown in Figure 4d–i. The mapping revealed a nearly uniform distribution of all the elements in the heterojunction. The dimensional analysis of the CN/NCS composite was obtained through the TEM analysis. C_3N_5 material is revealed to be of amorphous nature, and $NiCo_2S_4$ has an irregular-type arrangement. The TEM image for the CN/NCS composite, as shown in Figure 4j, clearly shows that the $NiCo_2S_4$ nanoparticles are uniformly dispersed on lamellar

sheets of C_3N_5. C_3N_5 has a two-dimensional lamellar structure with an irregular size in nano-dimension. The $NiCo_2S_4$ nanoparticles are found to be in range of 50–75 nm in diameter (particles measured by version 1.52A). The nearly spherical $NiCo_2S_4$ nanoparticles can be seen in intimate contact with two dimensional C_3N_5 sheets. The sheet-like structure of C_3N_5 and the particles attached to it can also be clearly seen in the TEM image shown in Figure S5. The lattice fringes for $NiCo_2S_4$ are clearly visible in the HRTEM image of the heterojunction (Figure 4k), inferring the high crystallinity of the heterojunction. As C_3N_5 is not highly crystalline, its lattice fringes are not observed in the HRTEM image.

3.5. XPS Analysis

The surface chemical states and elemental composition of the $NiCo_2S_4$ and $C_3N_5/NiCo_2S_4$ samples were further investigated by XPS analysis. The XPS survey spectra of NCS and 50CN/NCS are shown in Figure 5a. The XPS survey spectrum of the 50CN/NCS heterojunction revealed the presence of C, N, O, Ni, Co, S, and Cu elements in the photocatalyst. The presence of oxygen is attributed to the partial oxidation of $NiCo_2S_4$ during the synthesis process and the surface oxygen present in the sample [39]. A slight shifting in elemental characteristic peaks is observed. For the detailed analysis of all of the elements, the core-level spectra of Co2p, Ni2p, and S2p of both $NiCo_2S_4$ and $C_3N_5/NiCo_2S_4$ are compared.

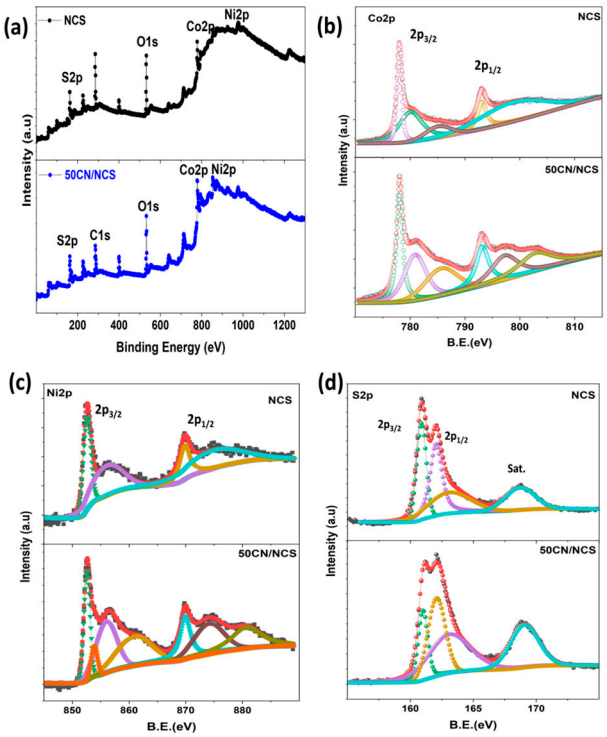

Figure 5. (**a**) Survey scan spectrum for $NiCo_2S_4$ (NCS) and $50C_3N_5/NiCo_2S_4$ (50CN/NCS) catalyst, (**b**) deconvoluted core-level Co2p spectra, (**c**) Core-level Ni2p spectra, and (**d**) S2p spectra for NCS and 50CN/NCS catalyst.

The C1s spectrum for pure C_3N_5 is deconvolved into two peaks, 284.7 and 287.5 eV, which are ascribed to sp^3 (C-C) and sp^2-hybridized carbon (N=C-N), respectively (Figure S6). Further, a small peak at a higher binding energy, 406.5 eV, corresponds to a π-electron peak characteristic of C_3N_5. This is because the n–π* transition is promoted by a higher number of unshared electron pairs due to increased nitrogen content [40]. Figure 5b presents the Co2p spectra for both the NCS and 50CN/NCS heterojunction. As illustrated in Co2p spectra for the NCS sample, Co2p spectra are divided into two spin–orbit doublets $2p_{3/2}$ and $2p_{1/2}$ levels. The major peak at the binding energy 778.08 corresponds to Co^{3+} states, while 780.18 eV is attributed to the Co^{2+} state of the Co atom [41]. The other peaks observed at 785.58 and

801.88 eV are identified as satellite peaks associated with the $2p_{3/2}$ and $2p_{1/2}$ levels [42]. Furthermore, for the sample 50CN/NCS, the binding energies of the peaks are slightly shifted to a higher energy side at 778.10, 780.92, 758.68, 793.19, 797.23, and 802.88 eV, respectively. In the case of Ni2p spectra, the peaks of the $NiCo_2S_4$ spectra centered at 856.10 and 875.03 eV are associated with Ni^{3+}, whereas the peaks at 852.6 and 869.86 eV are related to Ni^{2+} [43]. In the case of the 50CN/NCS sample, the peaks are observed at 852.59, 853.88, 856.01, 860.82, 869.88, and 880.65 eV, respectively (Figure 5c). The observed results indicate the shifting of the peaks for 50CN/NCS to a lower binding energy side as compared to the NCS sample, indicating the formation of a successful heterojunction between $NiCo_2S_4$ and C_3N_5. The negative and positive shifts in the binding energies of the elements in the heterojunction as compared to bare C_3N_5 and $NiCo_2S_4$ are indicative of increased/decreased electron densities, which confirms the electron transfer at the interface of the heterojunction. As shown in Figure 5d, the S2p spectra for $NiCo_2S_4$, the peak at 160.87eV and 162.03 eV, are attributed to the $2p_{3/2}$ and $2p_{1/2}$ states, revealing the Ni-S and Co-S bonding in the sample [44]. The other observed peaks are shakeup peaks associated with $2p_{3/2}$ and $2p_{½}$ orbital levels. The binding energy of the S2p peaks for 50CN/NCS is also changed, indicating the integration of $NiCo_2S_4$ and C_3N_5 to form a heterojunction.

3.6. NOR Degradation Analysis

For the selection of the best catalyst, the designed heterojunctions CN/NCS and individual materials' photocatalytic activity were examined against the norfloxacin (NOR) drug in a photochemical reactor under the illumination of a visible light source. Figure 6a shows the photocatalytic performance of various materials towards NOR when exposed to visible light in a 120 min experiment. The initial experimental conditions of NOR concentration = 20 ppm, catalyst dosage = 20 mg, and solution pH = 6 were selected for the experiment. The pure CN and NCS materials showed only a smaller amount of photocatalytic efficiency, which is 46.7% and 53.3%, respectively in 120 min of light exposure. On the heterojunction formation, i.e., with 10%CN content (10CN/NCS), the performance was Improved to 65.5%. The highest NOR degradation was achieved for 50CN/NCS heterojunction, i.e., 86.5% in 120 min. Clearly, the 50CN/NCS heterojunction is most effective under visible light towards the NOR degradation, achieving the highest efficiency. At the lower content of C_3N_5 in the heterojunction, the NOR degradation performance is low because of the low numbers of heterojunctions formed. In the lower content of CN, the major part of the heterojunction is $NiCo_2S_4$, which, though it has high absorbance in the visible region, it suffers with higher recombination. On the other hand, the heterojunction 50CN/NCS with a 1:1 ratio of CN and $NiCo_2S_4$ provides a sufficient number of heterojunctions and active centers for NOR degradation. The improved NOR degradation using $50C_3N_5/NiCo_2S_4$ indicates that the integration of C_3N_5 and $NiCo_2S_4$ results in the efficient separation of charge carriers, thereby increasing the photocatalytic efficiency of catalyst. Additionally, the experimental data were interpreted by a pseudo-first-order kinetic formulation, i.e., $\ln(C_0/C_t) = kt$, to quantitatively assess the photo-degradation rate as shown in Figure 6b. k is the photo-degradation rate constant, and C_0 and C are the concentration of NOR at time 0 and t, respectively. The usefulness of the first-order kinetic model is confirmed by the strong linear relationship between ln (C_0/C) and irradiation time (t). The apparent rate constant was determined from the kinetics plot (Figure 6c). The rate constant for the 50CN/NCS heterojunction was found to be 0.02904 $min^{-1,}$ which is 3.27 times higher than C_3N_5 and 2.8 times higher than the $NiCo_2S_4$ catalysts.

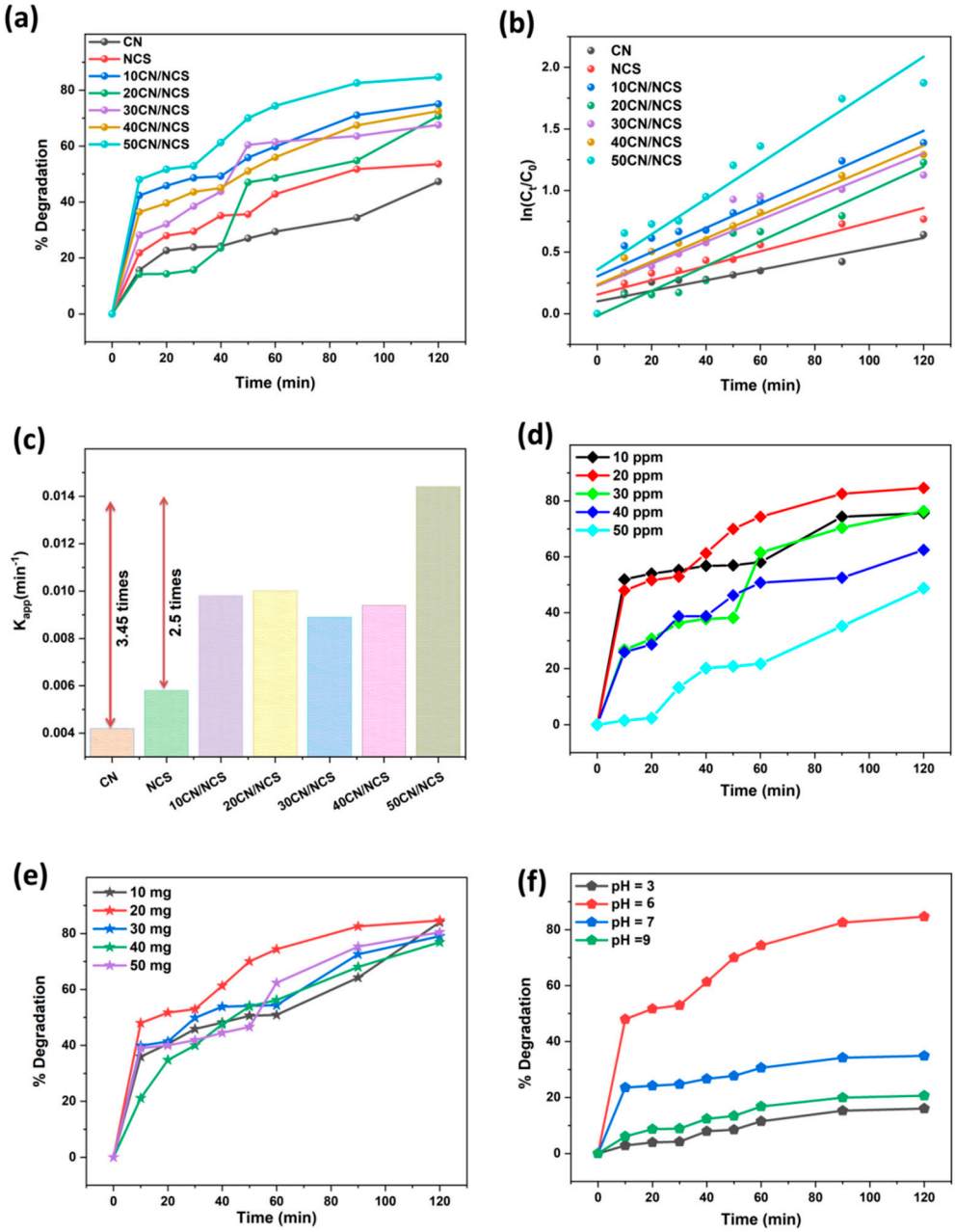

Figure 6. (**a**) Photocatalytic performance of different photocatalysts towards NFX degradation under visible light; (**b**) Kinetic plots of reactions using different photocatalysts; (**c**) rate constant observed for all synthesized catalysts; effect of (**d**) NFX concentration, (**e**) Catalyst dosage, and (**f**) Solution pH.

The reaction conditions and operational parameters are important as they govern the photocatalyst performance of the material. The amount of catalyst used, i.e., catalyst dosage, and the initial pollutant concentration, as well as the initial pH, are all the variables that affect photocatalytic removal efficiency [45]. The effect of various NOR concentrations on the 50CN/NCS heterojunction's photocatalytic efficiency was examined. Figure 6d displays the photodegradation efficiency of 50CN/NCS at different NOR concentrations. The removal efficiency of norfloxacin decreased with the increase in the initial NOR concentration beyond the optimum level. The photocatalytic degradation of NOR at 10, 20, 30, 40, and 50 ppm was found to be 78.6%, 86.5%, 81.3%, 65.4%, and 52.7%, respectively. The degradation increased when the initial NOR concentration was increased from 10 ppm to 20 ppm but decreased thereafter. With the increase in the initial NOR concentration, the photocatalyst surface becomes saturated, and the exposure of photons and catalyst

surfaces is also inhibited. Therefore, there are lesser active sites for adsorption, which lowers the catalyst's effectiveness. Figure 6e shows the impact of various catalyst dosages on photocatalytic activity for NOR degradation. The catalyst dosage was varied from 10 mg to 50 mg. The degradation efficiencies of NOR using 10, 20, 30, 40, and 50 mg of CN/NCS were 83.0%, 86.5%, 79.0%, 72.8%, and 73.4%, respectively. The photocatalytic degradation of NOR was increased when increasing the catalyst dosage from 10 mg to 20 mg. However, the removal efficiency of NOR was not significantly enhanced by further increasing the dosage of CN/NCS. At a higher dosage, light scattering occurs, which reduces the catalytic effectiveness. The higher content of the photocatalyst in solution leads to agglomeration, blocking the active reaction sites in the process [46]. Furthermore, it is crucial to understand how pH affects the photodegradation activity because it has a significant impact on the reaction by regulating the electrostatic interaction between solvent molecules, substrate, catalyst surface, and free radical production. The effect of pH on NOR degradation was studied at different values ranging from 3.0 to 9.0 as shown in Figure 6f. When the initial pH value of the NOR solution was 3.0, 6.0, 7.0, and 9.0, the degradation efficiency for NOR was found to be 16.06%, 86.5%, 42.8%, and 24.6%, respectively. The highest degradation was achieved at pH = 6.0, which is also the natural pH value of the NOR solution. The pH-dependent chemistry of NOR may be responsible for the variations in degradation efficiency. Inevitably, in acidic (pH < 6) and alkaline (pH > 7) settings, the breakdown capability was considerably hampered. It has been reported that the NOR displayed varied ionization conditions at different pH levels, with two dissociation constants (pK_{a1}) of 6.34 and (pK_{a2}) 8.75 [47]. The NOR exists in an anionic form at pH > 8.75, although it is considered cationic at pH 6.34, and it can exist in amphoteric circumstances at pH 6.34 to pH 8.75. The pzc of 50CN/NCS heterojunction was determined to be 5.4 (Figure S7). At working pH = 6, the 50CN/NCS heterojunction surface is negatively charged; on the other hand, the pollutant molecules exist mainly in a cationic form, favoring the electrostatic attraction. The degradation is extremely low in acidic conditions because the electrostatic repulsions between 50CN/NCS (positively charged) and the protonated NOR reduce adsorption activity under severe acidic circumstances. The electrostatic repulsion between the two negative surfaces will be restored under strong alkaline conditions. In the other direction, favorable adsorption may be accomplished at mild acidic to mild basic conditions, leading to better NOR destruction capability. Additionally, it was found that the UV–Vis absorption spectra of NOR altered under various pH circumstances due to the presence of various molecular configurations under various pH circumstances [48]. Albini and Monti have also reported the change in its physicochemical properties with the speciation of NOR [49]. In a further series of experiments, the photocatalytic potential of 50CN/NCS heterojunction was also tested for the degradation of other pollutants such as ciprofloxacin (CIP), sulfadiazine (SDZ), and bisphenol A (BPA), keeping the other operational parameters the same, i.e., [catalyst] = 20 mg, [pollutant] = 20 ppm, and pH = 6. The degradation efficiency plots are shown in Figure S8. The degradation efficiency was 89.1%, 78.3%, and 93.2% for CIP, SDZ, and BPA, respectively. The difference in degradation efficiencies is due to their different structure and different pKa values, i.e., pKa = 9.6 (BPA), ciprofloxacin (pKa: 6.09 and 8.62), and sulfadiazine (pKa 6.5). Thus, the 50CN/NCS heterojunction photocatalyst shows excellent results for other pollutants too.

3.7. Photocatalytic Mechanism and Reusability Analysis

To analyze the reasons for the superior photocatalytic performance of the CN/NCS heterojunction, band structure analysis, PL investigation, and electrochemical experiments were performed. A photoluminescence (PL) investigation was used to determine the recombination rate of photoexcited charge pairs, with high emission intensities indicating high recombination probability. Pure C_3N_5 exhibits a high intensity peak at 414 nm, as shown in Figure 7a. On the heterojunction formation with $NiCo_2S_4$, i.e., 50CN/NCS exhibited highly diminished PL intensities (flattened curve) than bare CN. The low PL intensity indicates a higher photoinduced charge carrier separation, which coincides well

with the photocatalytic efficacy of the catalyst [50]. The Z-scheme transfer between CN and NCS leads to higher separation. Further charge transfer efficiency was tested by conducting electrochemical and photoelectrochemical experiments, i.e., electrochemical impedance spectroscopy (EIS). The EIS Nyquist plots of the bare CN, NCS, and 50CN/NCS heterostructure samples are shown in Figure 7b. In general, a lesser Nyquist arc radius means better electron conductivity. Clearly, the 50CN/NCS nanohybrid's Nyquist plot arc radius is substantially lower than that of pure CN and NCS, indicating a quicker separation and transferability of photoexcited charge carriers. Further, the photocurrent response (PCR) analysis for the photocatalysts was performed (Figure 7c) to a typical continuous on–off schedule of visible light exposure. The photocurrent responsiveness of 50CN/NCS is improved over pure CN, which may be ascribed to the presence of interfaces between CN and $NiCo_2S_4$, where radiative charge carriers can be efficiently separated and photogenerated carrier recombination inhibited. As a result, higher photocatalytic activity can arise via the greater transfer efficiency of radiative electron–hole pairs. In order to predict the photocatalytic mechanism, the band structures of CN and NCS and the arrangement of bands in the heterojunction should be determined and analyzed in light of the photocatalytic performance. In this context, the flat band potential of both C_3N_5 and $NiCo_2S_4$ were determined from the analysis of Mott–Schottky plots [51]. The obtained E_{fb} values for CN and NCS were −0.91 V vs. Ag/AgCl and −0.32V vs. Ag/AgCl, respectively (Figure 8a,b). Thus, the conduction bands, which generally lie approx. 0.2 V below the CB for a n-type semiconductor, were found to be −1.11 and −0.52V vs. Ag/AgCl for CN and NCS, respectively. The E_{CBs} for CN and NCS are thus calculated as −0.91 and −0.32V vs. NHE. The valence band edge was determined using the equation $E_{VB} = E_{CB} + E_g$. The valence bands for both CN and NCS were found to be 1.04 V and 1.50 V vs. NHE, respectively. Thus, they form a staggered arrangement (Figure 8c).

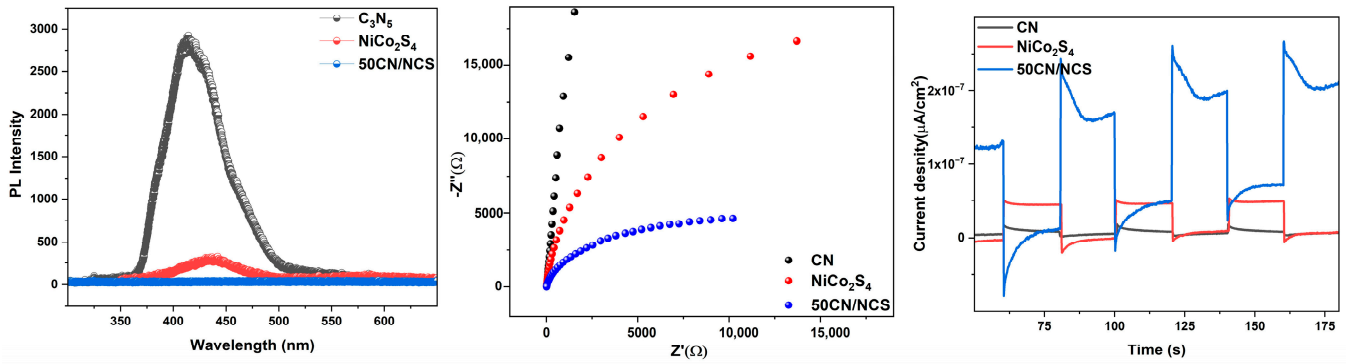

(**a**) (**b**) (**c**)

Figure 7. (**a**) Photoluminescence spectra, (**b**) EIS (Nyquist plots) spectra, and (**c**) transient photocurrent response for CN, NCS, and 50CN/NCS photocatalyst.

Radical trapping investigations were used to determine the active species responsible for the breakdown of NOR during photocatalytic reaction with the 50CN/NCS heterojunction. The sample solution was supplemented with EDTA, IPA, and p-BQ in order to quench the h^+, $^{\bullet}OH$, and $^{\bullet}O_2^-$, respectively, for the assessment of reactive oxygen species. By incorporating the appropriate scavengers into the solution of NOR in the presence of the photocatalyst, the producing capacity of active species was examined. Figure 9a displays the outcomes of the photocatalytic NOR removal in the presence of various radical scavengers. The majority of NOR degradation is inhibited by the addition of BQ, which causes only 28.5% degradation. The photocatalytic efficiency is also visibly suppressed by the addition of EDTA, which causes 47.3% NOR degradation followed by 56.1% for IPA. The results clearly revealed that $^{\bullet}O_2^-$ was the prime reactive species responsible for NOR degradation.

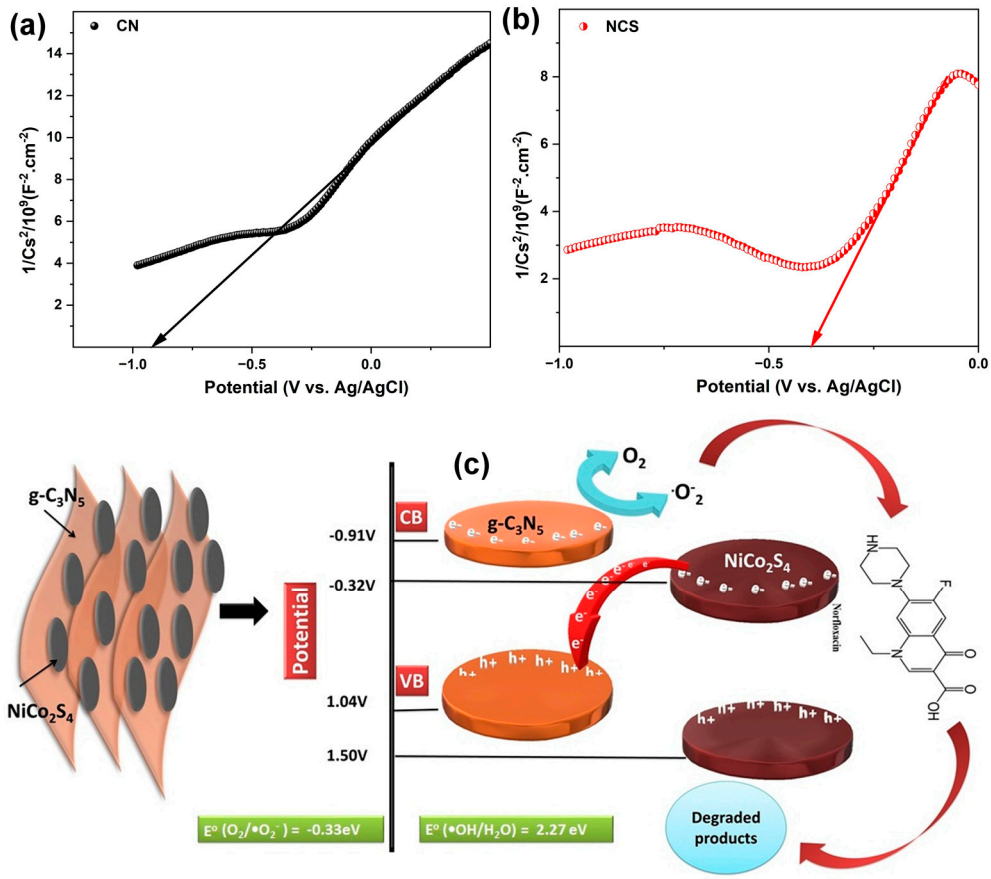

Figure 8. Mott–Schottky plots of (**a**) g-C_3N_5 and (**b**) $NiCo_2S_4$. (**c**) Proposed Z-scheme mechanism for norfloxacin degradation.

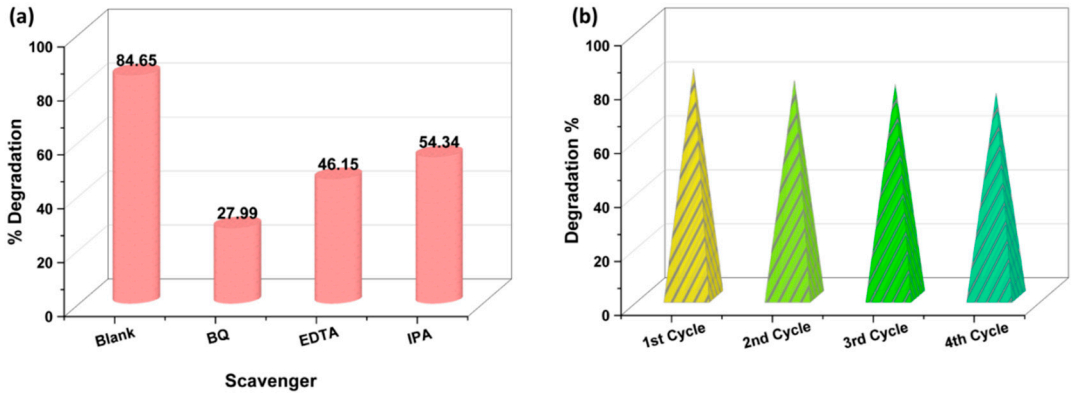

Figure 9. (**a**) Scavenging experiment for the determination of active radicals. (**b**) Reusability analysis of 50CN/NCS heterojunction.

By combining the results of the scavenging experiments and band structure/arrangement analysis, the Z-scheme mechanism appears to be more favorable. The proposed mechanism is shown in Figure 8c. Under the illumination of light, the generation of photogenerated carriers takes place in the conduction band and valence band of both C_3N_5 and $NiCo_2S_4$. Considering the excellent performance of the heterojunction, a type-II mechanism is ruled out. According to the type-II mechanism, the photogenerated electrons would migrate from CB of C_3N_5 towards that of NCS (−0.32 V) and would lose potential to generate $O_2^{-\bullet}$ radicals as $E^{\circ}(O_2/\cdot O_2^{-})$ (−0.33 eV) [52]. Similarly, the holes in the low-potential VB of CN could not generate •OH radicals. Thus, ruling out type-II mechanism, a Z-scheme mechanism is proposed based on the

band structure arrangement, scavenging experiment results, and shifts in the binding energies in the XPS measurements. The CB of C_3N_5 (E_{cb} = −0.91 eV) is much more negative than required for generation of superoxide anion radicals; hence, the thermodynamic feasibility of the generation of superoxide radical anions is quite high. The electrons forming the CB of $NiCo_2S_4$ (−0.32 V) may move to the VB of C_3N_5 (E_{vb} = 1.04 eV) via a Z-scheme transfer and recombine, leaving the photogenerated electrons accumulated in the CB of C_3N_5 (−0.91 V). Hence, there is a high thermodynamic feasibility of the generation of $O_2^{-\bullet}$ radicals as supported by the scavenging experiment results. Also, the negative and positive shifts in the B.E on junction formation confirms the Z-scheme transfer. The transfer is beneficial for charge carriers' separation and also in the protection of electrons and holes in high-potential CB and VB for better redox capability. There is a possibility that h^+ may cause the oxidation of water molecules to form $^\bullet$OH radicals. However, the E_{vb} of $NiCo_2S_4$ has a slightly positive potential than the generation of $^\bullet OH/H_2O$ (2.27 eV) [53], which rules out the role of $^\bullet$OH radicals in degradation mechanisms. Such results are also supported by the scavenging experiments that reveal the role of $^\bullet O_2^-$ radicals as the primary reactive species taking part in the degradation of pollutants.

Additionally, to ensure the stability and reusability of synthesized photocatalysts, which are the prime factors required for their practical utilization, a photocatalytic experiment was performed for four consecutive cycles with the recovered 50CN/NCS catalyst. After each run, the 50CN/NCS catalyst was separated and cleaned with deionized water multiple times before being dried in a vacuum oven for the next run. Figure 9b demonstrates the performance of the 50N/NCS heterojunction for NOR removal for four consecutive cycles. The removal efficiency for the second cycle slightly falls to 84.3% from 86.5%. The degradation efficiency reached 79.5% after the fourth cycle, indicating the stable nature and reusability of the catalyst. Further, metal leaching tests for Co and Ni elements in the 50CN/NCS heterojunction photocatalyst were conducted for two consecutive cycles of NOR degradation (Figure S9). The analysis was carried out with ICP-MS, i.e., inductively coupled plasma-mass spectrometry (Agilent 8800 ICP-QQQ). Negligible leaching rates of 0.02% and 0.013% for Co and Ni, respectively, during the first cycle were found. Interestingly, metal leaching was reduced to negligible for cycle 2. These extremely low negligible leaching and reusability experiments suggest the robustness of the material and a consistent photocatalytic performance. Table 1 shows the comparison of the performance of the 50CN/NCS heterojunction with other related heterojunctions from the literature. Thus, it can be observed that the 50CN/NCS heterojunction performs extremely well.

Table 1. Comparison of 50CN/NCS heterojunction photocatalytic performance with some related heterojunctions from the literature.

Photocatalyst	Source of Illumination	Pollutant/Concentration	Catalyst Dose	Irradiation Time	Efficiency	Ref.
$CoTiO_3/g\text{-}C_3N_4$	Low-power light source (26 W)	Tetracycline hydrochloride/10 ppm	200 mg	60 min	79.6%	[54]
$g\text{–}C_3N_4\text{–}ZnZrO_3$	500 W Xe lamp/400 nm optical filter	Norfloxacin	20 mg	180 min	96%	[55]
$g\text{-}C_3N_5/BiVO_4/CoFe\text{–}LDH$	Xenon lamp 300 W Xe lamp/400 nm optical filter	Norfloxacin/10 ppm	600 mg + PMS	120 min	95.3%	[56]
$BiVO_4/g\text{-}C_3N_4$	26 W Exo Terra Natural Light	Ciprofloxacin/10 ppm	100 mg	60 min	78.2%	[57]
$g\text{-}C_3N_5/Ti_3C_2$	300 W Xe lap/400 nm optical filter	Tetracycline/10 ppm	30 mg	60 min	81.6%	[58]
$ZnO/NiCo_2S_4$	1000 W halogen lamp/visible light	Doxycycline/40 ppm	20 mgL^{-1}	150 min	99%	[59]
$C_3N_5/NiCo_2S_4$ (50CN/NCS)	500 W Xe lamp/400 nm optical filter	Norfloxacin/20 ppm	20 mg	120 min	86.5%	This work

3.8. Degradation Pathway for Norfloxacin (NOR)

Because of the extremely active and non-selective characteristics of the reactions between the radicals and organic pollutants, which may dramatically assemble the toxicity of primary substances, photocatalysis frequently produces an array of intermediates. Potential photocatalytic degradation mechanisms of NOR in the $C_3N_5/NiCo_2S_4$ system are suggested in light of the discovered intermediate materials and the relevant literature. Based on the literature and intermediates detected through LC–MS (Figure S10), three different pathways are proposed (Scheme 1).

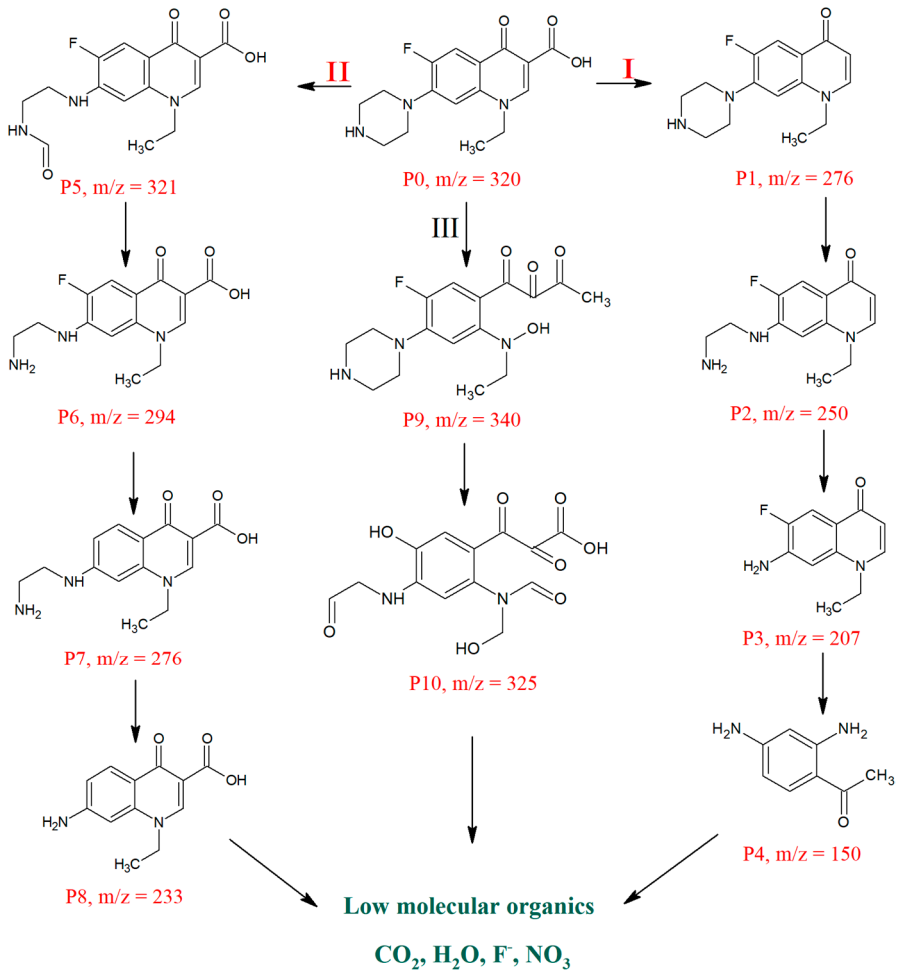

Scheme 1. Plausible degradation pathway of norfloxacin using $C_3N_5/NiCo_2S_4$ heterojunction.

Decarboxylation (-CO_2) from the initial molecule initiates the first pathway (I) and yields the product P1 (m/z = 276). In the next step, the piperazine ring is partially eliminated to produce the product P2 (m/z = 250) [60]. The products P3 (m/z = 207) and P4 (m/z = 150) are created as a consequence of the further cleavage of the piperazine ring-rupturing processes, which is comparable to the results of the reported findings [61]. In the second degradation pathway (II), NOR may also be effectively oxidized to create the product P5 (m/z = 321). The removal of the carbonyl group from P5 gave the product P6 (m/z = 294) [62]. P6 was converted into P7 (m/z = 276) through the defluorination reaction, and P7 was further oxidized to give P8 (m/z = 233) [63,64]. In pathway III, the double bond in the quinoline ring was broken down through the $^{\bullet}O_2^-$/hydroxyl radical oxidation to obtain the product P9 (m/z = 340). As per the band-structure analysis, the hydroxyl radical generation was not thermodynamically feasible at the VB. However, the scavenging experiments reveal that superoxide radical anions are the main active species with little contribution from $OH^{\bullet}$ radicals. The alternative way of the generation of hydroxyl radicals is shown in Scheme 2 (favored by working pH = 6).

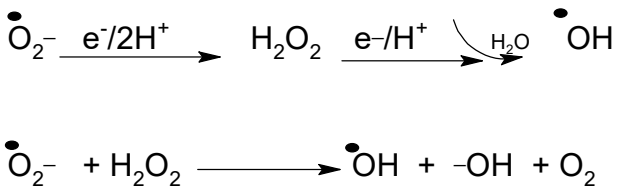

Scheme 2. Alternative route for generation of $^{\bullet}OH$ radicals.

Further defluorination and oxidation gave the product P10 (m/z = 325) [65]. It is evident that the NOR molecule is progressively broken down by losing its groups, leading to its mineralization into CO_2, H_2O, and some inorganic ions [66,67]. The mineralization was further confirmed by a total organic carbon (TOC) analysis, and the results are provided in Figure S11. During NOR degradation by the 50CN/NCS sample, 39.2% TOC removal was achieved in 1 h, which increased to 65% in the 3 h experiment. High TOC removal efficiency suggests mineralization, which continues to increase further [66,67].

4. Conclusions

Photocatalysts that are reliable and effective have long been required for the development of highly efficient reactive systems to clean up contaminated water systems. In this study, we developed a novel Z-scheme heterojunction photocatalyst, $C_3N_5/NiCo_2S_4$, through an in-situ hydrothermal strategy. The optimized heterojunction 50CN/NCS exhibited an excellent norfloxacin removal efficiency of 86.5% in 120 min under visible light. The primary causes of this are the formation of a Z-scheme heterojunction between C_3N_5 and $NiCo_2S_4$, which effectively encourages charge carrier separation and strong redox capability. The reusability and metal leaching tests confirmed the robustness, and the consistent 50CN/NCS hybrid demonstrated exceptional photodegradation performance. The junction also exhibited superior performance for other pollutants, such as ciprofloxacin, sulfadiazine, and bisphenol A. Furthermore, $\bullet O_2^-$ was the prime reactive oxygen species involved in the photocatalytic reduction of norfloxacin. A plausible NOR degradation route was also proposed. This research contributes to the designing of an efficient Z-scheme heterojunction photocatalysts in addition to suggesting an innovative photocatalytic framework for the detoxification of wastewater.

Supplementary Materials: The following supporting information can be downloaded at: https://www.mdpi.com/article/10.3390/chemistry6050056/s1, Figure S1: Digital pictures of C_3N_5 and g-C_3N_4 showing the color difference; Figure S2: XRD pattern of C_3N_5; Figure S3: Tauc plots for (a) C_3N_5 (b) $NiCo_2S_4$ and (c) 50CN/NCS heterojunction; Figure S4: Elemental mapping and spatial distribution of elements in 50CN/NCS heterojunction; Figure S5: TEM image for 50CN/NCS heterojunction; Figure S6: Deconvoluted XPS spectra –C1s and N1s for C_3N_5; Figure S7: pzc determination for 50CN/NCS heterojunction; Figure S8: Photocatalytic degradation of other pollutants over 50CN/NCS heterojunction; Figure S9: Metal leaching tests under 50CN/NCS + visible light system; Figure S10: LC-MS spectra for NOR degradation obtained after 15 min of experiment with 50CN/NCS heterojunction; Figure S11: TOC removal for NOR degradation with 50CN/NCS heterojunction under visible light.

Author Contributions: S.R.: investigation, visualization, software, data curation, validation, and writing—first draft. A.K.: conceptualization, resources, formal analysis, methodology, software, supervision, and writing—first draft. T.W.: supervision, resources, formal analysis, project administration, and writing—review and editing. P.D. and G.S.: investigation and validation. H.S.: writing—review and editing. All authors have read and agreed to the published version of the manuscript.

Funding: This work was supported by the Key Research and Development Program of Shaanxi Province (2023-LL-QY-42 and 2024NC-ZDCYL-02-05), the Xi'an University of Architecture and Technology Research Initiation (grant program (1960323102)), the Xi'an University of Architecture and Technology, the Special Program for the Cultivation of Frontier Interdisciplinary Fields (X20230079), and the Open Fund for the Key Laboratory of Soil and Plant Nutrition of Ningxia (ZHS202401).

Data Availability Statement: Data will be available on request.

Conflicts of Interest: The authors declare no conflicts of interest.

References

1. Zhang, S.; Li, B.; Wang, X.; Zhao, G.; Hu, B.; Lu, Z.; Wen, T.; Chen, J.; Wang, X. Recent developments of two-dimensional graphene-based composites in visible-light photocatalysis for eliminating persistent organic pollutants from wastewater. *Chem. Eng. J.* **2020**, *390*, 124642. [CrossRef]
2. Liu, J.; Dong, Y.; Liu, Q.; Liu, W.; Lin, H. MoS_2-based nanocomposites and aerogels for antibiotic pollutants removal from wastewater by photocatalytic degradation process: A review. *Chemosphere* **2024**, *354*, 141582. [CrossRef] [PubMed]
3. Sharma, V.K.; Johnson, N.; Cizmas, L.; McDonald, T.J.; Kim, H. A review of the influence of treatment strategies on antibiotic resistant bacteria and antibiotic resistance genes. *Chemosphere* **2016**, *150*, 702–714. [CrossRef] [PubMed]
4. Khan, I.; Liu, W.; Zada, A.; Raziq, F.; Ali, S.; Shah, M.I.A.; Ateeq, M.; Khan, M.; Alei, D.; Fazil, P.; et al. Recent progress in emerging materials and hybrid nanocomposites for peroxymonosulfate and peroxydisulfate activation towards solar light-driven photocatalytic degradation of emerging pollutants. *Coord. Chem. Rev.* **2024**, *499*, 215466. [CrossRef]
5. Mehrizad, A.; Gharbani, P. Removal of methylene blue from aqueous solution using nano-TiO2/UV process: Optimization by response surface methodology. *Prog. Color Color. Coat.* **2016**, *9*, 135–143.
6. Ma, R.; Zhang, S.; Wen, T.; Gu, P.; Li, L.; Zhao, G.; Niu, F.; Huang, Q.; Tang, Z.; Wang, X. A critical review on visible-light-response CeO_2-based photocatalysts with enhanced photooxidation of organic pollutants. *Catal. Today* **2019**, *335*, 20–30. [CrossRef]
7. Mehrizad, A.; Gharbani, P. Optimization of operational variables and kinetic modeling for photocatalytic removal of Direct Blue 14 from aqueous media by ZnS nanoparticles. *J. Water Health* **2017**, *15*, 955–965. [CrossRef]
8. Xu, S.; Li, M.; Wang, Y.; Jin, Z. Enhanced photocatalytic hydrogen evolution over coal-based carbon quantum dots modified $CoMoO_4$/g-C_3N_4. *Int. J. Hydrogen Energy* **2024**, *51*, 16–30. [CrossRef]
9. Ayodhya, D.; Veerabhadram, G. A review on recent advances in photodegradation of dyes using doped and heterojunction based semiconductor metal sulfide nanostructures for environmental protection. *Mater. Today Energy* **2018**, *9*, 83–113. [CrossRef]
10. Ji, H.; Zhang, L.; Hu, C. Chemical-bond conjugated $BiO(OH)_xI_{1-x}$-AgI heterojunction with high visible light activity and stability in degradation of pollutants. *Appl. Catal. B Environ.* **2017**, *218*, 443–451. [CrossRef]
11. Lin, J.; Tian, W.; Guan, Z.; Zhang, H.; Duan, X.; Wang, H.; Sun, H.; Fang, Y.; Huang, Y.; Wang, S. Functional Carbon Nitride Materials in Photo-Fenton-Like Catalysis for Environmental Remediation. *Adv. Funct. Mater.* **2022**, *32*, 2201743. [CrossRef]
12. Mane, G.P.; Talapaneni, S.N.; Lakhi, K.S.; Ilbeygi, H.; Ravon, U.; Al-Bahily, K.; Mori, T.; Park, D.H.; Vinu, A. Highly ordered nitrogen-rich mesoporous carbon nitrides and their superior performance for sensing and photocatalytic hydrogen generation. *Angew. Chem. Int. Ed.* **2017**, *56*, 8481–8485. [CrossRef] [PubMed]
13. Kim, I.Y.; Kim, S.; Premkumar, S.; Yang, J.H.; Umapathy, S.; Vinu, A. Thermodynamically stable mesoporous C_3N_7 and C_3N_6 with ordered structure and their excellent performance for oxygen reduction reaction. *Small* **2020**, *16*, 1903572. [CrossRef] [PubMed]
14. Ma, S.; Yang, D.; Li, B.; Guan, Y.; Wu, M.; Wu, J.; Guo, Y.; Sheng, L.; Liu, L.; Yao, T. An interfacial C-S bond bridged S-scheme ZnS/C_3N_5 for photocatalytic H_2 evolution: Opposite internal-electric-field of ZnS/C_3N_4, increased field strength, and accelerated surface reaction. *J. Colloid Interface Sci.* **2024**, *664*, 960–971. [CrossRef]
15. Jing, B.; Ao, Z.; Zhao, W.; Xu, Y.; Chen, Z.; An, T. Evaluation procedure of photocatalysts for VOCs degradation from the view of density functional theory calculations: gC_3N_4 dots/graphene as an example. *J. Mater. Chem. A* **2020**, *8*, 20363–20372. [CrossRef]
16. Teymourinia, H.; Alshamsi, H.A.; Al-nayili, A.; Gholami, M. Photocatalytic degradation of chlorpyrifos using Ag nanoparticles-doped g-C_3N_5 decorated with dendritic CdS. *Chemosphere* **2023**, *344*, 140325. [CrossRef] [PubMed]
17. Zhang, J.; Ding, Y.; Ma, X.; Liu, Y.; Zhang, L.; Wang, K.; Cao, S.; Xu, S. Constructing a Z-scheme heterojunction photocatalyst I-ABN-C_3N_4@CDs/BiOI by synergistically in situ modified g-C_3N_4 via carbon dots and copolymerization for BPA degradation. *Mater. Res. Bull.* **2024**, *170*, 112584. [CrossRef]
18. Asoubar, S.; Mehrizad, A.; Behnajady, M.A.; Ramazani, M.E.; Gharbani, P. Hexavalent chromium reduction and Rhodamine B degradation by visible-light-driven photocatalyst of stannum indium sulfide-samarium vanadate. *npj Clean Water* **2023**, *6*, 27. [CrossRef]
19. Cao, Y.; Guan, Y.; Zhang, Y.; Zhao, T.; Ding, W.; Hui, W.; Wu, J. Construction of P-C_3N_4/C_3N_5 isotypic heterojunction for effective degradation of organic pollutants. *J. Taiwan Inst. Chem. Eng.* **2023**, *150*, 105019. [CrossRef]
20. He, S.; Liu, Y.; Wang, G.; Luo, L.; Tang, X.; Xiang, D.; Jiang, T.; Jing, J.; Wang, L. Heterojunction photocatalyst FeS_2/g-C_3N_5 for activating sulfites to degrade tetracycline: A stable degradation system based on heterogeneous processes. *Environ. Res.* **2023**, *237*, 116939. [CrossRef]
21. Xu, H.; Wang, D.; Ma, J.; Zhang, T.; Lu, X.; Chen, Z. A superior active and stable spinel sulfide for catalytic peroxymonosulfate oxidation of bisphenol S. *Appl. Catal. B Environ.* **2018**, *238*, 557–567. [CrossRef]
22. Zhu, Y.; Ji, X.; Wu, Z.; Liu, Y. $NiCo_2S_4$ hollow microsphere decorated by acetylene black for high-performance asymmetric supercapacitor. *Electrochim. Acta* **2015**, *186*, 562–571. [CrossRef]
23. Li, J.; Wan, Y.; Li, Y.; Yao, G.; Lai, B. Surface Fe(III)/Fe(II) cycle promoted the degradation of atrazine by peroxymonosulfate activation in the presence of hydroxylamine. *Appl. Catal. B Environ.* **2019**, *256*, 117782. [CrossRef]
24. Resende Leite, R.; Colombo, R.; Eduardo Bimbi, F., Jr.; Roberto de Vasconcelos Lanza, M.; da Silva Barud, H.; Ramos Moreira Afonso, C.; Inês Basso Bernardi, M. Precursor effect on the hydrothermal synthesis of pure ZnO nanostructures and enhanced photocatalytic performance for norfloxacin degradation. *Chem. Eng. J.* **2024**, *496*, 154374. [CrossRef]

25. Liu, T.; Yang, G.; Wang, W.; Wang, C.; Wang, M.; Sun, X.; Xu, P.; Zhang, J. Preparation of C_3N_5 nanosheets with enhanced performance in photocatalytic methylene blue (MB) degradation and H2-evolution from water splitting. *Environ. Res.* **2020**, *188*, 109741. [CrossRef]
26. Ito, K.; Noda, K. Highly efficient hydrogen production and selective CO_2 reduction by the C_3N_5 photocatalyst using only visible light. *Phys. Chem. Chem. Phys.* **2024**, *26*, 153–160. [CrossRef]
27. Golub, F.S.; Beloshapkin, S.; Gusel'nikov, A.V.; Bolotov, V.A.; Parmon, V.N.; Bulushev, D.A. Boosting Hydrogen Production from Formic Acid over Pd Catalysts by Deposition of N-Containing Precursors on the Carbon Support. *Energies* **2019**, *12*, 3885. [CrossRef]
28. Chang, X.; Li, W.; Liu, Y.; He, M.; Zheng, X.; Bai, J.; Ren, Z. Hierarchical $NiCo_2S_4$@NiCoP core-shell nanocolumn arrays on nickel foam as a binder-free supercapacitor electrode with enhanced electrochemical performance. *J. Colloid Interface Sci.* **2019**, *538*, 34–44. [CrossRef]
29. Wan, H.; Jiang, J.; Yu, J.; Xu, K.; Miao, L.; Zhang, L.; Chen, H.; Ruan, Y. $NiCo_2S_4$ porous nanotubes synthesis via sacrificial templates: High-performance electrode materials of supercapacitors. *CrystEngComm* **2013**, *15*, 7649–7651. [CrossRef]
30. Zhang, J.; Jing, B.; Tang, Z.; Ao, Z.; Xia, D.; Zhu, M.; Wang, S. Experimental and DFT insights into the visible-light driving metal-free C_3N_5 activated persulfate system for efficient water purification. *Appl. Catal. B Environ.* **2021**, *289*, 120023. [CrossRef]
31. Li, S.; Wang, C.; Cai, M.; Liu, Y.; Dong, K.; Zhang, J. Designing oxygen vacancy mediated bismuth molybdate (Bi_2MoO_6)/N-rich carbon nitride (C_3N_5) S-scheme heterojunctions for boosted photocatalytic removal of tetracycline antibiotic and Cr(VI): Intermediate toxicity and mechanism insight. *J. Colloid Interface Sci.* **2022**, *624*, 219–232. [CrossRef] [PubMed]
32. Kumar, P.; Vahidzadeh, E.; Thakur, U.K.; Kar, P.; Alam, K.M.; Goswami, A.; Mahdi, N.; Cui, K.; Bernard, G.M.; Michaelis, V.K.; et al. C_3N_5: A Low Bandgap Semiconductor Containing an Azo-Linked Carbon Nitride Framework for Photocatalytic, Photovoltaic and Adsorbent Applications. *J. Am. Chem. Soc.* **2019**, *141*, 5415–5436. [CrossRef] [PubMed]
33. Li, Z.; Zhou, Y.; Zhou, Y.; Wang, K.; Yun, Y.; Chen, S.; Jiao, W.; Chen, L.; Zou, B.; Zhu, M. Dipole field in nitrogen-enriched carbon nitride with external forces to boost the artificial photosynthesis of hydrogen peroxide. *Nat. Commun.* **2023**, *14*, 5742. [CrossRef] [PubMed]
34. Zhu, T.; Zhang, G.; Hu, T.; He, Z.; Lu, Y.; Wang, G.; Guo, H.; Luo, J.; Lin, C.; Chen, Y. Synthesis of $NiCo_2S_4$-based nanostructured electrodes supported on nickel foams with superior electrochemical performance. *J. Mater. Sci.* **2016**, *51*, 1903–1913. [CrossRef]
35. Chen, H.; Zhao, L.; Fang, W.; Li, W.; He, X.; Zhang, F. Construction of hierarchical $NiCo_2S_4$ nanowires on 3D biomass carbon for high-performance supercapacitors. *J. Mater. Sci. Mater. Electron.* **2018**, *29*, 9573–9581. [CrossRef]
36. Yin, H.; Cao, Y.; Fan, T.; Zhang, M.; Yao, J.; Li, P.; Chen, S.; Liu, X. In situ synthesis of Ag_3PO_4/C_3N_5 Z-scheme heterojunctions with enhanced visible-light-responsive photocatalytic performance for antibiotics removal. *Sci. Total Environ.* **2021**, *754*, 141926. [CrossRef]
37. Mortazavi, B.; Shojaei, F.; Shahrokhi, M.; Azizi, M.; Rabczuk, T.; Shapeev, A.V.; Zhuang, X. Nanoporous C_3N_4, C_3N_5 and C_3N_6 nanosheets; novel strong semiconductors with low thermal conductivities and appealing optical/electronic properties. *Carbon* **2020**, *167*, 40–50. [CrossRef]
38. Sahoo, M.K.; Sharma, S.; Mishra, V.; Ghosh, T.K.; G, R.R. MoO_3 thin layers on $NiCo_2S_4$ substrate for efficient electrochemical charge storage. *Nanotechnology* **2020**, *31*, 414003. [CrossRef]
39. Li, C.; Liang, Y.; Lu, Z.; Xiang, X.; Ying, L.; Wang, H. $NiCo_2S_4$ decorated g-C_3N_4 nanosheets for enhanced photocatalytic hydrogen evolution. *J. Nanoparticle Res.* **2020**, *22*, 41. [CrossRef]
40. Li, C.; Zhang, J.; Chen, X.; Tao, H.; Zhou, Y.; Zhu, M. Upgraded charge transfer by an internal electric field in 2D/2D BiOCl/N-rich C_3N_5 heterojunctions for efficiently visible-light catalytic NO removal. *Chem. Eng. J.* **2023**, *468*, 143753. [CrossRef]
41. Li, C.; Du, S.; Wang, H.; Naghadeh, S.B.; Allen, A.L.; Lin, X.; Li, G.; Liu, Y.; Xu, H.; He, C.; et al. Enhanced visible-light-driven photocatalytic hydrogen generation using $NiCo_2S_4$/CdS nanocomposites. *Chem. Eng. J.* **2019**, *378*, 122089. [CrossRef]
42. Li, Z.; Xu, J.; Liu, Z.; Liu, X.; Xu, S.; Ma, Y. 2D $NiCo_2S_4$ decorated on $ZnIn_2S_4$ formed S-scheme heterojunction for photocatalytic hydrogen production. *Int. J. Hydrogen Energy* **2023**, *48*, 3466–3477. [CrossRef]
43. Wu, J.; Huang, X.; Xia, X. Exploring $NiCo_2S_4$ nanosheets arrays by hydrothermal conversion for enhanced high-rate batteries. *J. Energy Chem.* **2019**, *35*, 132–137. [CrossRef]
44. Peng, J.; Xu, J.; Wang, Z.; Ding, Z.; Wang, S. Developing an efficient $NiCo_2S_4$ cocatalyst for improving the visible light H_2 evolution performance of CdS nanoparticles. *Phys. Chem. Chem. Phys.* **2017**, *19*, 25919–25926. [CrossRef]
45. Dhiman, P.; Rana, G.; Alshgari, R.A.; Kumar, A.; Sharma, G.; Naushad, M.; Alothman, Z.A. Magnetic Ni–Zn ferrite anchored on g-C_3N_4 as nano-photocatalyst for efficient photo-degradation of doxycycline from water. *Environ. Res.* **2023**, *216*, 114665. [CrossRef]
46. Saeed, M.; Alwadai, N.; Farhat, L.B.; Baig, A.; Nabgan, W.; Iqbal, M. Co_3O_4-Bi_2O_3 heterojunction: An effective photocatalyst for photodegradation of rhodamine B dye. *Arab. J. Chem.* **2022**, *15*, 103732. [CrossRef]
47. Jabbar, Z.H.; Graimed, B.H.; Alsunbuli, M.M.; Sabit, D.A. Developing a magnetic bismuth-based quaternary semiconductor boosted by plasmonic action for photocatalytic detoxification of Cr(VI) and norfloxacin antibiotic under simulated solar irradiation: Synergistic work and radical mechanism. *J. Alloys Compd.* **2023**, *958*, 170521. [CrossRef]
48. Ao, X.; Wang, W.; Sun, W.; Lu, Z.; Li, C. Degradation and transformation of norfloxacin in medium-pressure ultraviolet/peracetic acid process: An investigation of the role of pH. *Water Res.* **2021**, *203*, 117458. [CrossRef]
49. Albini, A.; Monti, S. Photophysics and photochemistry of fluoroquinolones. *Chem. Soc. Rev.* **2003**, *32*, 238–250. [CrossRef]

50. Dhiman, P.; Sharma, J.; Kumar, A.; Sharma, G.; Dawi, E.A. Photocatalytic degradation of malachite green by waste derived bio-char impregnated Bi_5O_7Br/Fe_3O_4 magnetic composite. *Opt. Mater.* **2023**, *146*, 114568. [CrossRef]
51. Lan, Y.; Luo, Y.; Yu, S.; Ye, H.; Zhang, Y.; Xue, M.; Sun, Q.; Yin, Z.; Li, X.; Xie, C.; et al. Cornstalk hydrochar produced by phosphoric acid-assisted hydrothermal carbonization for effective adsorption and photodegradation of norfloxacin. *Sep. Purif. Technol.* **2024**, *330*, 125543. [CrossRef]
52. Kumar, A.; Rana, A.; Sharma, G.; Dhiman, P. Incorporating Bi nanodots into $CuBi_2O_4/CuFe_2O_4$ heterojunction for a wide spectral synchronous photoreduction of hexavalent chromium and degradation of imidacloprid. *Opt. Mater.* **2023**, *140*, 113876. [CrossRef]
53. Dhiman, P.; Mehta, T.; Kumar, A.; Sharma, G.; Naushad, M.; Ahamad, T.; Mola, G.T. $Mg_{0.5}Ni_xZn_{0.5}$-xFe_2O_4 spinel as a sustainable magnetic nano-photocatalyst with dopant driven band shifting and reduced recombination for visible and solar degradation of Reactive Blue-19. *Adv. Powder Technol.* **2020**, *31*, 4585–4597. [CrossRef]
54. Le, M.-V.; Nguyen, Q.-T.-N.; Huynh, N.-D.-T.; Pham, N.-D.; Truong, C.-H.; Tran, H.-T.; Le, P.-N.-M.; Ngo, T.-H.; Huynh, H.T. Direct Z-scheme $CoTiO_3/g$-C_3N_4 nanoparticles: Fabrication and application as a photocatalyst for degradation of tetracycline hydrochloride assisted by peroxydisulfate or peroxymonosulfate under simulated sunlight. *Nanotechnol. Environ. Eng.* **2023**, *8*, 675–690. [CrossRef]
55. Zhu, Z.; Tang, L.; Ban, Y.; Li, H. Hydrothermal synthesis of Step-scheme layer g-C_3N_4/columnar $ZnZrO_3$ heterojunction photocatalyst toward efficient norfloxacin degradation under solar light. *J. Solid State Chem.* **2024**, *337*, 124815. [CrossRef]
56. Lee, E.; Jagan, G.; Choi, J.U.; Cha, B.; Yoon, Y.; Saravanakumar, K.; Park, C.M. Peroxymonosulfate-activated photocatalytic degradation of norfloxacin via a dual Z-scheme g-$C_3N_5/BiVO_4$/CoFe−LDH heterojunction: Operation and mechanistic insights. *Chem. Eng. J.* **2024**, *494*, 152961. [CrossRef]
57. Tran, T.-H.; Le, P.-N.-M.; Ngo, T.-H.; Huynh, N.-D.-T.; Oh, W.-C.; Le, M.-V. An investigation on the visible light-driven Z-scheme $BiVO_4/g$-C_3N_4 heterostructures: Performance, evaluation, and mechanism for dye and antibiotics degradation. *Mater. Today Commun.* **2024**, *40*, 109373. [CrossRef]
58. Guan, Y.; Cao, Y.; Ma, S.; Yang, Y.; Zhao, T.; Zhang, Y.; Xin, B.; Wu, J.; Guo, Y. Metal-free g-C_3N_5 photocatalyst coupling MXenes Ti_3C_2 for tetracycline degradation: Insight for electron transfer mechanism, degradation mechanism and photothermal effect. *J. Alloys Compd.* **2023**, *951*, 169864. [CrossRef]
59. Swedha, M.; Okla, M.K.; Al-amri, S.S.; Alaraidh, I.A.; Al-ghamdi, A.A.; Mohebaldin, A.; Abdel-Maksoud, M.A.; Aufy, M.; Studenik, C.R.; Thomas, A.M.; et al. Green synthesis of two-electron centre based $ZnO/NiCo_2S_4$ QDs-OVs using Punica granatum fruit peel extract for an exceptional visible light photocatalytic degradation of doxycycline and ciprofloxacin. *Chemosphere* **2022**, *304*, 135225. [CrossRef]
60. Li, J.; Xia, Z.; Ma, D.; Liu, G.; Song, N.; Xiang, D.; Xin, Y.; Zhang, G.; Chen, Q. Improving photocatalytic activity by construction of immobilized Z-scheme $CdS/Au/TiO_2$ nanobelt photocatalyst for eliminating norfloxacin from water. *J. Colloid Interface Sci.* **2021**, *586*, 243–256. [CrossRef]
61. Gou, J.; Ma, Q.; Deng, X.; Cui, Y.; Zhang, H.; Cheng, X.; Li, X.; Xie, M.; Cheng, Q. Fabrication of Ag_2O/TiO_2-Zeolite composite and its enhanced solar light photocatalytic performance and mechanism for degradation of norfloxacin. *Chem. Eng. J.* **2017**, *308*, 818–826. [CrossRef]
62. Chen, Q.; Hao, Y.; Song, Z.; Liu, M.; Chen, D.; Zhu, B.; Chen, J.; Chen, Z. Optimization of photocatalytic degradation conditions and toxicity assessment of norfloxacin under visible light by new lamellar structure magnetic ZnO/g-C_3N_4. *Ecotoxicol. Environ. Saf.* **2021**, *225*, 112742. [CrossRef]
63. Guo, J.; Shen, C.H.; Sun, J.; Xu, X.J.; Li, X.Y.; Fei, Z.H.; Liu, Z.T.; Wen, X.J. Highly efficient activation of peroxymonosulfate by Co_3O_4/Bi_2MoO_6 pn heterostructure composites for the degradation of norfloxacin under visible light irradiation. *Sep. Purif. Technol.* **2021**, *259*, 118109. [CrossRef]
64. Zhang, C.; Jia, M.; Xu, Z.; Xiong, W.; Yang, Z.; Cao, J.; Peng, H.; Xu, H.; Xiang, Y.; Jing, Y. Constructing 2D/2D N-ZnO/g-C_3N_4 S-scheme heterojunction: Efficient photocatalytic performance for norfloxacin degradation. *Chem. Eng. J.* **2022**, *430*, 132652. [CrossRef]
65. Yu, Y.; Yao, L.; Bai, M.; Ji, Z.; Li, J.; Huang, X. Oh mineralization of norfloxacin in the process of algae bloom water treatment in a drinking water treatment system Of 12,000 M3 Per Day. *Chem. Eng. J.* **2019**, *360*, 1355–1362. [CrossRef]
66. Wang, T.; Shi, H.; Kumar, A.; Zhang, D.; Wang, H.; Wang, S.; Zheng, J. Efficient visible-light photocatalysis of chloramphenicol using novel engineered biochar-based Ti-doped Bi_2WO_6 composite: Mechanisms, degradation pathways, and applications. *Sep. Purif. Technol.* **2024**, *332*, 125780. [CrossRef]
67. Wang, T.; Zheng, J.; Cai, J.; Liu, Q.; Zhang, X. Visible-light-driven photocatalytic degradation of dye and antibiotics by activated biochar composited with K^+ doped g-C_3N_4: Effects, mechanisms, actual wastewater treatment and disinfection. *Sci. Total Environ.* **2022**, *839*, 155955. [CrossRef]

Disclaimer/Publisher's Note: The statements, opinions and data contained in all publications are solely those of the individual author(s) and contributor(s) and not of MDPI and/or the editor(s). MDPI and/or the editor(s) disclaim responsibility for any injury to people or property resulting from any ideas, methods, instructions or products referred to in the content.